Beyond Fresnel's approximation: Luneburg's kernel to simulate the interferometric images of droplets or irregular rough particles

Marc Brunel, Emmanuel Porcheron, Pascal Lemaitre, Jeroen van Beeck, Rosaria Vetrano, Gérard Gréhan, Sébastien Coëtmellec

Version of Record: https://www.sciencedirect.com/science/article/pii/S0030401822003340
Manuscript_8b0e1e24f47e59150f4434a38f8d6e77

Beyond Fresnel's approximation : Luneburg's kernel to simulate the interferometric images of droplets or irregular rough particles

Marc Brunel[1,*], Emmanuel Porcheron[2], Pascal Lemaitre[2], Jeroen van Beeck[3], Rosaria Vetrano[4], Gérard Gréhan[5], Sébastien Coëtmellec[1]

[1] *UMR CNRS 6614 CORIA, Université de Rouen Normandie, Avenue de l'Université, BP 12, 76801 Saint-Etienne du Rouvray Cedex, France,*
[2] *Institut de Radioprotection et de Sürété Nucléaire (IRSN), BP 68, 91192 Gif-sur-Yvette, France*
[3] *Institut van Karman, B-1640 Rhode-Saint-Genese, Belgium*
[4] *KU Leuven, Dpt of Mechanical Engineering, Leuven, B-3001, Belgium*
[5] *RainbowVision, Déville-lès-Rouen, 76250, France*

** marc.brunel@coria.fr*

Abstract

Interferometric particle imaging is generally interpreted in the framework of Fresnel conditions. We develop here a new formalism based on Luneburg's kernel. It enables to predict the interferometric images of droplets or rough particles when Fresnel conditions are not respected. It is compared to previous experimental results, and then used to understand possible sources of noise when analyzing interferometric particle images.

I - Theoretical formulation

Interferometric imaging offers an interesting solution to the characterization of droplets, bubbles or irregular rough particles in a flow. Particles are illuminated by a laser, while a CCD sensor records the scattered interferometric images. They can be two-wave interference patterns in the case of droplets or bubbles [1-14], or speckle patterns in the case of more complex particles [15-22]. In this last case, there is a priori no theoretical model that can predict rigorously these patterns. This is particularly true in the case of particles whose shape's modelling itself remains an important challenge. We can cite ice crystals whose growth modelling is an important domain of research [23]. Nevertheless, assuming that the particles can be assimilated to a collection of point emitters randomly located all over the contour of the rough particle, it can be demonstrated that the 2Dimensional-Fourier transform of the interferometric pattern is directly linked to the 2 Dimensional-autocorrelation of the spatial repartition of the emitters on the scattering particles [15,16]. This can be written mathematically as follows:

$$|FT_{2D}[I(x,y)](\lambda\, B_{tot}\, u, B_{tot}\, v)| \propto |A_{2D}[G_0(x_0,y_0)](\Delta x,\Delta y)| \qquad (1)$$

$I(x,y)$ is the intensity (interferometric image recorded on the sensor), (x,y) are the transverse coordinates in the plane of this image). λ is the laser wavelength, B_{tot} the B-coefficient of the optical transfer matrix from the particle to the sensor, (u,v) are the spectral coordinates after 2D-Fourier transformation of the interferometric pattern. $G_0(x_0,y_0)$ is the electric field scattered by the particle (assumed to be an ensemble of point emitters). (x_0,y_0) are the transverse coordinates in the plane of the particle. $(\Delta x,\Delta y)$ are the coordinates after 2D-autocorrelation of function G_0. This relation has been validated experimentally in many cases [16,19-22] (and references enclosed). It is actually established using a scalar Huygens-Fresnel formalism. It is thus limited to the domain where Fresnel conditions are valid. As applications of the technique could be numerous, it is important to study the limits of validity of this relation (1). For this purpose, it appears crucial to develop a numerical simulator that is not limited to the sole Fresnel conditions.

Diffraction can be described using different theories, with different levels of approximations as in Fresnel or Rayleigh-Sommerfeld (RS) formalisms. The difference between RS and Fresnel integrals lies in the inclination factor with the optical axis, taken into account in the RS solution, and in the development of the amplitude of spherical waves of the type $\frac{e^{i\,k\,r}}{r}$. In Fresnel's model, the radial coordinate $r=\sqrt{x^2+y^2+z^2}$ is approached by a first order development $r\approx z+\frac{x^2+y^2}{2\,z}$ that generates a quadratic phase term versus the transverse coordinates x and y. This quadratic phase term, typical of Fresnel's kernel, is very convenient to describe light propagation through complete optical systems, using generalized Fresnel integrals and eventually the expansion of an hard-aperture over a basis of Gaussian functions [9].

Unfortunately, this formalism can not describe cases where the observation point is close to the diffracting screen. This problem can be solved using the Rayleigh-Sommerfeld (RS) solution where the phase term is not approximated using the first order development of the radial coordinate r. In Interferometric Particle Imaging systems, the scattering particles are in general far from the imaging objective, and we imagine first that Fresnel conditions are always satisfied. Nevertheless, the sensor is in a defocused position, with a defocus parameter that can be small. The distance between the focused image of the particle and the observation point can be so small that Fresnel conditions are actually not respected.

Our objective is double in this study: first we want to develop an analytical model that can be applied both when Fresnel conditions are respected or not. There are indeed cases where the interferometric images suffer alterations that can not be interpreted in the Fresnel approximation. Section II will show such an exemple. Secondly, we want to develop a vectorial IPI model that can simulate correctly IPI experiments taking into account the polarization of light. It will indeed become a necessary tool to develop and analyze polarization-resolved IPI experiments.

Luneburg addressed with high attention the resolution of the Helmoltz equation [24]. Fresnel's kernel appears as a first order Taylor series expansion of the Luneburg's kernel in the far field approximation. Luneburg's description is well adapted through the definition of a specific kernel, in good accordance with the first-type RS integral. It can be easily applied to the modelling of IPI experiments, in the continuity of previous works that used the Fresnel kernel. As mentioned for the RS integral, there will be no approximation concerning the radial coordinate r. This formalism will offer the possibility to address our two objectives: (1) develop an efficient vectorial model for IPI, (2) apply the model in more general conditions than the sole Fresnel conditions. The inconvenience is that we will lose the capabilities offered by Fresnel integrals (generalized Fresnel integrals to describe

complete systems, and expansion of elements as hard-apertures over a basis of Gaussian functions because such functions are no more attractive).

The electric field scattered by the rough particle under laser illumination will be noted in the plane of the particle (z=0) : $\boldsymbol{E_0} = (E_0^x, E_0^y, E_0^z)$. According to Luneburg's development, the different components of the electromagnetic field: $\boldsymbol{E_{z_p}} = (E_{z_p}^x, E_{z_p}^y, E_{z_p}^z)$ at distance z_p of the particle can be obtained through [24-26]:

$$E_{z_p}^x(x,y,z_p) = -\frac{z_p}{2\pi} \iint E_0^x(\xi,\eta,0) \left(\frac{i\,k\,r-1}{r^3}\right) e^{i\,k\,r}\, d\xi\, d\eta \quad (2)$$

$$E_{z_p}^y(x,y,z_p) = -\frac{z_p}{2\pi} \iint E_0^y(\xi,\eta,0) \left(\frac{i\,k\,r-1}{r^3}\right) e^{i\,k\,r}\, d\xi\, d\eta \quad (3)$$

where $r^2 = (x-\xi)^2 + (y-\eta)^2 + {z_p}^2$, and $k = 2\pi/\lambda$. The longitudinal component is obtained by means of Maxwell's equation $div(\boldsymbol{E_z}) = 0$. We get:

$$E_{z_p}^z(x,y,z_p) = \frac{1}{2\pi} \iint \left[(x-\xi)\, E_0^x(\xi,\eta,0) + (y-\eta)\, E_0^y(\xi,\eta,0)\right] \left(\frac{i\,k\,r-1}{r^3}\right) e^{i\,k\,r}\, d\xi\, d\eta \quad (4)$$

As previously mentioned, there is no theoretical model that can calculate rigorously the electromagnetic field scattered by an irregular rough particle of any shape. In order to investigate the limits of relation (1) when Fresnel conditions are not respected, particles will be assimilated to a collection of point emitters located all over the contour of the rough particle (as in previous studies, which will make possible the comparisons).

Assuming that the electric field scattered by the particle is transverse to the propagation axis z, the electric field scattered by the particle will be written $\boldsymbol{E_0} = (E_0^x, E_0^y, 0)$, where the u-component (u = x or y) is given by :

$$E_0^u(x,y,z) = \sum_{i=1}^{N_{gp}} \alpha_{i,u}\, \delta(x-a_i, y-b_i, z-c_i)\, e^{i\,\varphi_{i,u}} \quad (5)$$

The δ are Dirac functions, N_{gp} is the number of emitting spots that cover the particle. (a_i, b_i, c_i) are the coordinates of point emitter numbered i. For the u-component (u = x or y), $\alpha_{i,u}$ is its amplitude, and $\varphi_{i,u}$ its phase. This expression of E_0^u describes irregular rough particles covered by scattering asperities, and droplets or bubbles as well, considering only two, three or four glare points [9,27,28]. Using relations (2-4), we can then determine the x-, y- and z- components of the electric field scattered at distance z_p of the center of the particle (center located at position z=0). We obtain for the x- and y-components:

$$E_{z_p}^u(x,y,z_p) = -\sum_{i=1}^{N_{gp}} \frac{z_p - c_i}{2\pi}\, \alpha_{i,u} \left(\frac{i\,k\,r_i-1}{r_i^3}\right) e^{i\,k\,r_i}\, e^{i\,\varphi_{i,u}} \quad (6)$$

where u = x or y, and $r_i = \sqrt{(x-a_i)^2 + (y-b_i)^2 + (z_p - c_i)^2}$.

The z-component is given by:

$$E_{z_p}^{z}(x,y,z_p) = \frac{1}{2\pi} \sum_{i=1}^{N_{gp}} \left[\alpha_{i,x}\,(x-a_i)\,e^{i\,\varphi_{i,x}} + \alpha_{i,y}\,(y-b_i)\,e^{i\,\varphi_{i,y}}\right] \left(\frac{i\,k\,r_i - 1}{r_i^3}\right) e^{i\,k\,r_i} \quad (7)$$

Finally, the intensity in the plane of the sensor ($z = z_p$) can be evaluated numerically, combining relations (6-7), from :

$$I(x,y,z_p) \propto \left|E_{z_p}^{x}(x,y,z_p)\right|^2 + \left|E_{z_p}^{y}(x,y,z_p)\right|^2 + \left|E_{z_p}^{z}(x,y,z_p)\right|^2 \quad (8)$$

Let us compare this development to Fresnel's formalism. Assuming that $c_i \approx 0$ and that $z_p \gg x, y, a_i, b_i$, we can write: $\frac{z_p - c_i}{2\pi}\ \alpha_{i,u} \left(\frac{i\,k\,r_i - 1}{r_i^3}\right) \approx \frac{i}{\lambda\,z_p}\alpha_{i,u}$ and simplify the phase term: $e^{i\,k\,r_i} \approx e^{i\,k\left[z_p + \frac{(x-a_i)^2}{2\,z_p} + \frac{(y-b_i)^2}{2\,z_p}\right]}$. In the case of an electric field with only one component, it leads to the scalar Fresnel model already used in previous studies [9,29,30]:

$$E_{z_p}^{Fresnel}(x,y,z_p) = -\sum_{i=1}^{N_{gp}} \frac{i}{\lambda\,z_p}\ \alpha_i\ e^{i\,k\left[z_p + \frac{(x-a_i)^2}{2\,z_p} + \frac{(y-b_i)^2}{2\,z_p}\right]} e^{i\,\varphi_i} \quad (9)$$

For comparison, with the notation $r = PM$, the first-type Rayleigh-Sommerfeld integral for diffraction $A(M) = -\frac{i}{\lambda}\iint_{(S)} A(P)\cos(\theta)\frac{1}{ik}\frac{d}{dPM}\left(\frac{e^{i\,k\,PM}}{PM}\right) d^2S(P)$ where $\cos(\theta) = \frac{z_p}{r}$ leads to the Luneburg's kernel of equations (2-3): $-\frac{z_p}{2\pi}\left(\frac{i\,k\,r - 1}{r^3}\right) e^{i\,k\,r}$.

In diffraction theory, the angular spectrum method is frequently used. The propagation of the angular spectrum $\widetilde{U}$ is described in Fresnel conditions by relation:

$$\widetilde{U}(u,v,z_p) = \widetilde{U}(u,v,0) \times e^{i\,k\,z_p - i\,\pi\,\lambda\,z_p\,(u^2+v^2)} \quad (10)$$

In Luneburg's condition, it respects the more accurate relation (see appendix B of reference [26]):

$$\widetilde{U}(u,v,z_p) = \widetilde{U}(u,v,0) \times e^{i\,z_p\,\sqrt{k^2 - 4\,\pi^2\,(u^2+v^2)}} \quad (11)$$

II - A comparison with experimental results

The previous model can be applied simply to spherical droplets. In this case, for a scattering angle of 66°, light scattered by the droplet is mainly composed of light reflected on the droplet (p=0 order in Debye series) and light refracted in the droplet without any additional internal reflexion within the droplet (p=1 order in Debye series). The electric field scattered by the droplet can be described by only two point emitters, the well-known glare points, i.e. $N_{gp} = 2$ in equation (5). Their exact positions (parameters a_i, b_i, c_i), and the phase difference (parameters φ_i) can be determined using geometrical optics. Their amplitudes are identical at 66° scattering angle, for a perpendicular polarization of the incident electric field. In these conditions, it is easy to compare results obtained using equation (6) based on Luneburg's kernel (limited to only one transverse component linked to the polarization of the illuminating laser field), and the scalar equation (8) using Fresnel's kernel.

In an ILIDS experiment [3], the interferometric particle image is obtained using an objective and a CCD sensor located in an out-of-focus plane. The previous vectorial model cannot describe the optical system as could be done using a generalized Huygens-Fresnel integral [9,29,30], because we are not in Fresnel conditions anymore. In order to make comparisons with experimental results obtained with a real ILIDS set-up, it is necessary to find an equivalent configuration without objective. Figure 1 explains this. The droplet is described by the two emitting glare points A and B. Their focused images are A' and B'. In the out-of-focus plane where the CCD is located, a pattern composed of two-wave interferences is observed. They are actually equivalent to those that would be created by two emitters A' and B' separated by Δ', at distance p of the sensor.

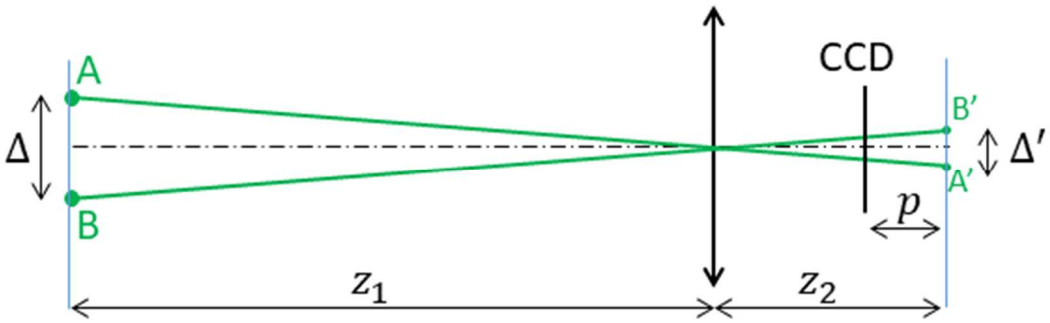

Figure 1: Equivalent set-up adapted to the developments performed

Let us consider an experimental case: the airborne ALIDS probe [31]. This instrument has been realized within the European Facility for Airborne Research (EUFAR) of Seventh framework program of the European Community to perform airborne measurements of the size of droplets. It has been presented in references [31] and the structure of the instrument is shown in figure 2.

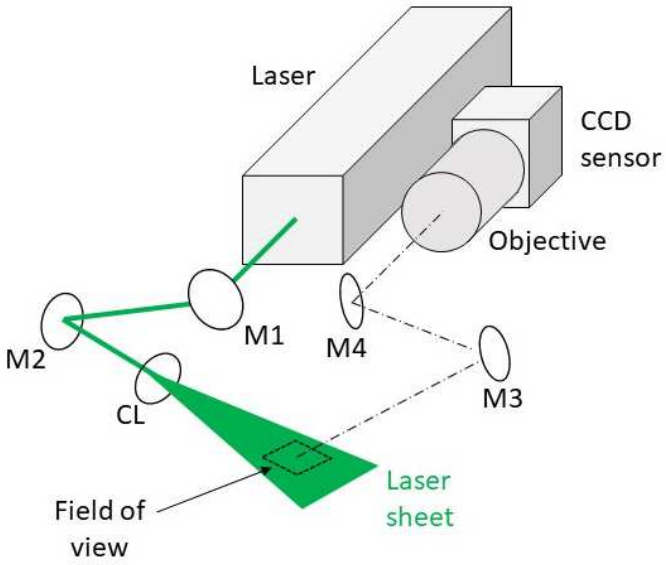

(a)

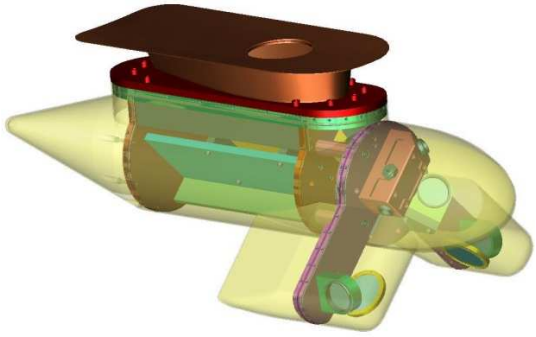

(b)

Figure 2: Principle of the ALIDS probe: M1, M2, M3, M4 are reflecting mirrors, CL is a cylindrical lens to generate a laser sheet (a), design of the final instrument (b) (see reference [31] for more details)

Despite optical windows due to the atmospheric environment, and deflecting mirrors that ensure a better compactness to the device, the optical set-up of this probe can be simplified to the one of figure 1, with $z_1 = 0.4m, f = 0.025m, (z_2 - p) = f = 0.025m$. The CCD sensor is in the focus plane of the objective in this instrument, but it works well in an out-of-focus configuration as the droplets are at a finite distance z_1 of the objective, in the plane of the laser sheet, and not at infinity. The CCD sensor is a 8-bit DALSA Genie HM1024 camera. The CCD resolution is 1024x768 pixels (pixel size of 7.4 μm). The laser is a frequency-doubled Quantel Ultra 100 laser emitting at 532 nm. In the configuration discussed here, we use a f/0.95 Goyo objective (focus length 25mm), which gives interferometric images with limited aberrations despite a large aperture. The set-up is a compromise between a relatively high working distance, a large field of view, and a size range measurement for water droplet diameters between 20 and 200 micrometers. The scattering angle of 66° induces image deformations that can be solved using a Scheimpflug system, or working in the focus plane of the imaging objective (this last solution is used in the ALIDS probe to limit the weight of the apparatus). This ensemble of compromises enabled to record interferometric images in flight. Using

the generalized Huygens-Fresnel formalism described in reference [9], that takes into account the whole imaging system (slices of air, the lens and its aperture [9,32,33]), figure 3(a) shows the interferometric image of two glare points A and B separated from $\Delta = 63\ \mu\text{m}$. It corresponds to a water droplet (refractive index 1.33) whose diameter is $70 \pm 1\ \mu\text{m}$ using a geometrical optics definition of the glare points. This interferometric configuration is equivalent to a two-wave interference pattern generated by two glare points A' and B' separated from $\Delta' = \frac{z_2}{z_1}\Delta = \frac{f}{z_1 - f}\Delta \approx 4.2\ \mu\text{m}$, and recorded in a plane at distance $\text{p} = \frac{f^2}{z_1 - f} \approx 0.0017\ \text{m}$ (these relations have been developed using the conjugation law through a lens). Figure 3(b) shows the interferometric pattern predicted for this equivalent configuration using equation (8) (adapted to Fresnel conditions) considering two glare points separated from $4.2\ \mu\text{m}$, at distance $z_p = 0.0017m$. This model does not describe the role of the aperture but the frequency of the fringes is exactly the same as the one of figure 3(a). Both models describe the same configuration in terms of interferometric pattern. We can note that z_p is only a few millimeters. As the CCD sensor is larger, the coordinates (x,y) in the plane of the sensor can be of the order of magnitude as z_p. It means that the set-up does not respect the Fresnel conditions when the aperture is large, and that the Luneburg development should be used ; Figure 3(c) shows thus the interferometric pattern predicted with the same assumptions as Fig 3(b) using now relation (6). We can observe that the fringes are not parallel lines but look like hyperbols.

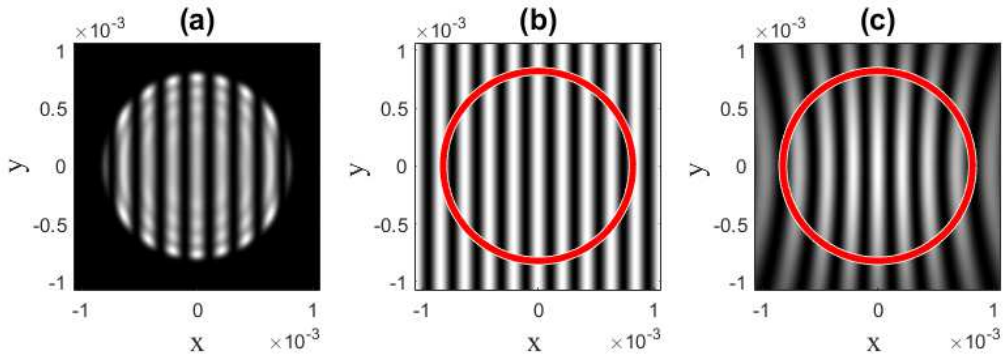

Figure 3: Interferometric image of two glare points A and B separated from $\Delta = 63\ \mu\text{m}$ (i.e. water droplet of diameter is $70 \pm 1\ \mu\text{m}$) using the model of reference [9] based on generalized Huygens Fresnel integrals (a), pattern predicted using equation (8) that does not describe the aperture (Fresnel kernel [29]) (b), and pattern predicted using now relation (6) (Luneburg kernel) (c).

Figure 4(a) shows a second example in the case of two glare points A and B separated from $\Delta = 162\ \mu\text{m}$ using the generalized Huygens-Fresnel formalism of reference [9]. It corresponds to a water droplet (refractive index 1.33) whose diameter is $180 \pm 1\ \mu\text{m}$. Figure 4(b) and 4(c) show the simulations predicted using Fresnel and Luneburg's kernels respectively in the case of the equivalent set-up (A' and B' separated from $\Delta' = 10.8\ \mu\text{m}$, with the same distance $z_p = 0.0017m$.

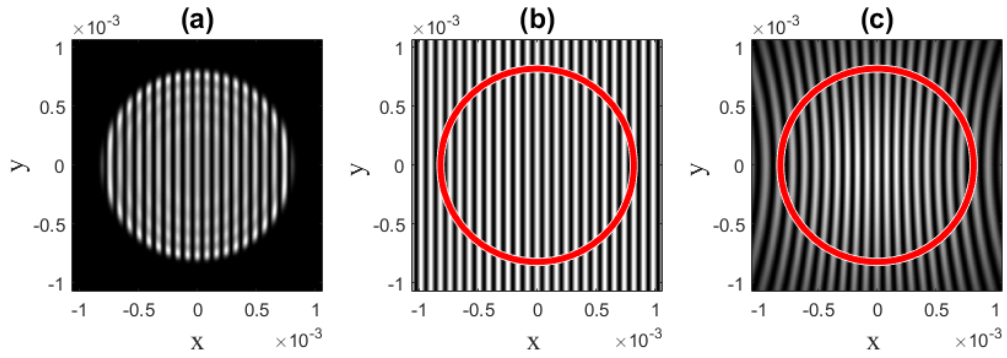

Figure 4: Interferometric image of two glare points A and B separated from $\Delta = 162\ \mu\mathrm{m}$ (i.e. water droplet of diameter is $180 \pm 1\ \mu\mathrm{m}$) using the model of reference [9] based on generalized Huygens Fresnel integrals (a), pattern predicted using equation (8) that does not describe the aperture (Fresnel kernel [29]) (b), and pattern predicted using now relation (6) (Luneburg kernel) (c).

The parameters used in these simulations are those of the airborne ALIDS probe [31]. Three experimental patterns recorded in flight or during laboratory tests with ALIDS are reported in figure 5 (a), (b) and (c). The diameter of the out-of-focus images, and the frequency of the fringes are well recovered using our simulations in the case of these droplets, whose sizes vary in the range from 70 micrometers to 180 micrometers approximately. Nevertheless, the fringes of these patterns are no more perfectly vertical in the border of the out-of-focus images. This behavior is only described using the Luneburg's formalism (simulations of figures 3(c) and 4(c)). In this configuration of the ALIDS probe, that uses a high-aperture f/0.95 Goyo objective, Fresnel conditions are no longer perfectly satisfied in the borders of the out-of-focus images. But the observations made can be interpreted using Luneburg's kernel that gives better predictions of the interferometric images.

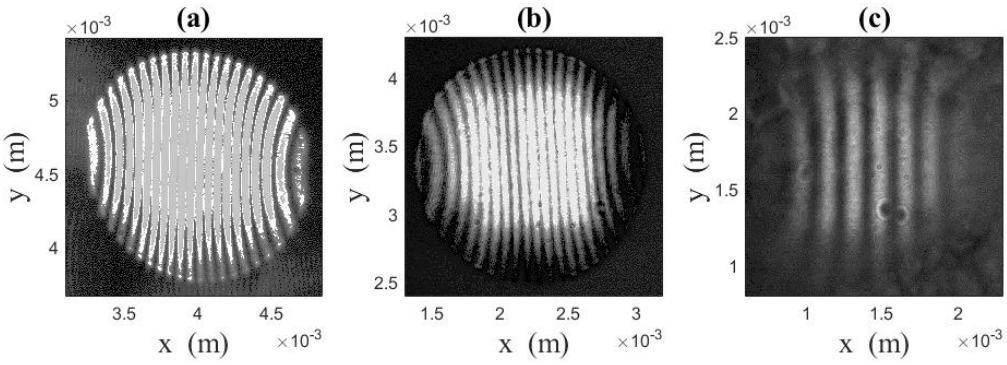

Figure 5: Experimental ILIDS patterns recorded with the ALIDS probe [31]. The set-up corresponds to the parameters of the simulations of figure 3 and 4.

III – Predictions for irregular rough particles: case of a cross-like particle

Let us now detail the modifications predicted in the case of irregular rough particles. We consider a cross-like particle, depicted in figure 6. It is composed of 200 point emitters randomly located on the two bars of the cross. Each bar is 60 micrometers long and 6 micrometers large. The normalized amplitude of each emitter is 1, while its phase is a random number in the range [0,2π].

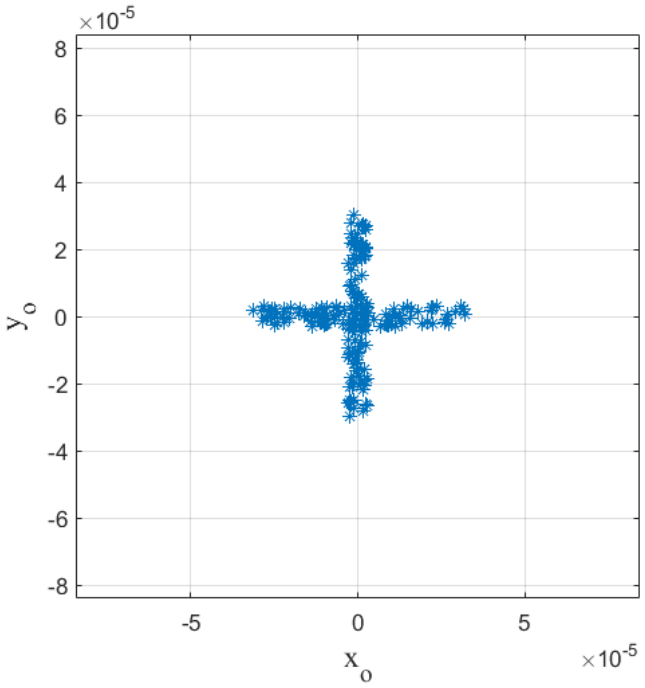

Figure 6: crossed-like particle composed of 200 point emitters

The wavelength of our simulations will be : $\lambda = 532\ nm$. Figure 7 shows the interferometric patterns (actually the absolute value of the electric field) predicted at distance $z_p = 0.02m$. Figure 7(a) has been obtained using the scalar Fresnel's model of equation (8) while figure 7(b) has been obtained using the vectorial Luneburg's model based on relations (6) and (7). Both patterns appear very similar. This is confirmed by figure 8(a) that shows the difference between the intensity obtained using Fresnel's model and the intensity obtained using Luneburg's model (normalized to 1). It appears clearly that both models give similar results in the center of the pattern. Differences appear in the surrounding ring.

As mentioned in section II, The model based on relations (6) and (7) does not describe the whole optical system, as depicted in figure 1, but an equivalent propagation in free space. It is interesting to give a system corresponding to previous simulations. For example, these simulations made at distance $z_p = 0.02m$ correspond to an equivalent IPI system with the following set of parameters : $z_1 = 0.2m,\ z_2 = 0.05m, f = 0.04m,\ p = z_p = 0.02m$, for cross-like rough particles of length $\Delta = 240\mu\text{m}$. We can verify that $\Delta'/\Delta = z_2/z_1$, while the conjugation law ${z_1}^{-1} + {z_2}^{-1} = f^{-1}$ is well respected.

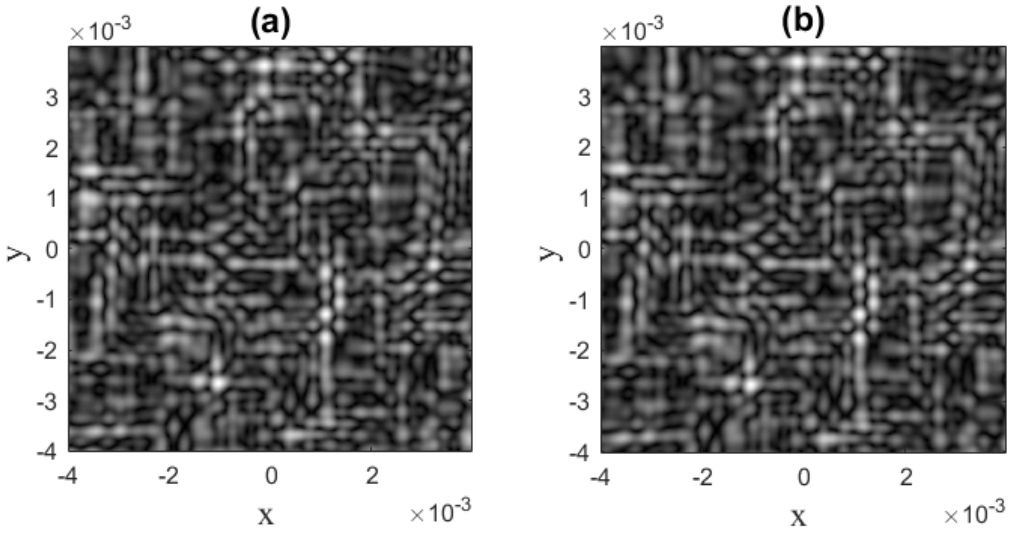

Figure 7: Interferometric images (actually the absolute value of the electric field for better contrast) of the cross-like particle of figure 6 using Fresnel's model (a) and Luneburg's model (b) at distance $z_p = 0.02m$.

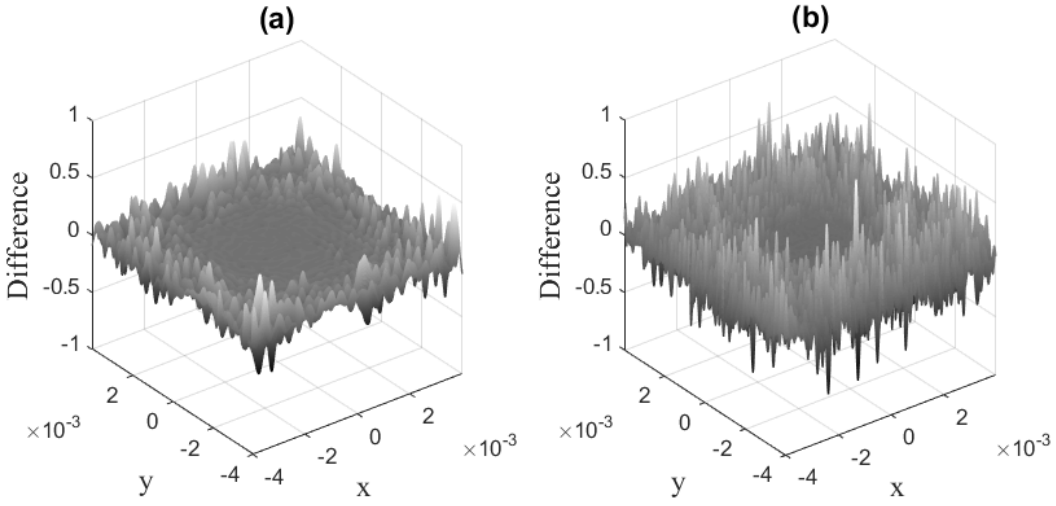

Figure 8: Normalized difference $\left|\frac{I_{Luneburg}(x,y)-I_{Fresnel}(x,y)}{I_{Luneburg}(x,y)}\right|$ when $z_p = 0.02m$ (a) and when $z_p = 0.01m$ (b).

Figure 9 shows now the interferometric patterns predicted at distance $z_p = 0.01m$. As previously, figure 9(a) has been obtained using the scalar Fresnel's model of equation (8) while figure 9(b) has been obtained using the vectorial Luneburg's model based on relations (6) and (7). Figure 8(b) shows the difference between the intensity obtained using Fresnel's model and the intensity obtained using Luneburg's model. Except in the center of the pattern, both models give different results. The pattern of figure 9(b) shows some distorted profile, as already observed in the case of droplets in section II. In the corners of the pattern of figure 9(b) where this « distortion » is the most visible, we have the $x = y = 4\ mm$ while $z_p = 1cm$. Fresnel conditions $z_p \gg x, y$ are clearly not respected and both models give different results.

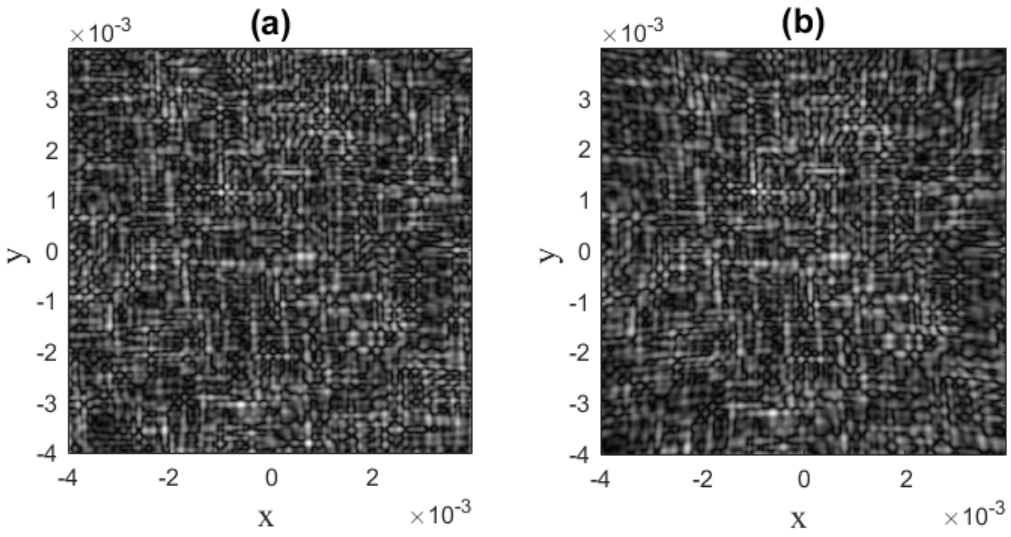

Figure 9: Interferometric images (actually the absolute value of the electric field) of the cross-like particle of figure 5 using Fresnel's model (a) and Luneburg's model (b) at distance $z_p = 0.01m$.

These differences can induce important effects on the analysis of the particle's shape. In a last example, figure 10 shows indeed the interferometric patterns predicted at distance $z_p = 0.005m$. Figure 10(a) has been obtained using the scalar Fresnel's model of equation (8) while figure 10(b) has been obtained using the vectorial Luneburg's model based on relations (6) and (7). Both patterns are now very different, except in the center. Some distorsion-like pattern is clearly evidenced on figure 10(b). From such interferometric patterns, an analysis of the particle's shape and size is done in general using relation (1). Unfortunately, this relation (1) is established in a Fresnel formalism. Let us first compare the results obtained using the sole truncated patterns in the blue rectangles of figure 10. Figure 11(a) shows the binarized 2D-Fourier transform of the central part of the interferometric pattern of figure 10(a) (selection of the pattern in the blue rectangle), while 11(b) shows the binarized 2D-Fourier transform of the central part of the interferometric pattern of figure 10(b). The scaling factor $\lambda\, B_{tot}$ has been applied in such a way that the axes of figure 11 can be assimilated to the coordinates in the plane of the particle according to relation (1). Parameter B_{tot} equals $z_p = 0.005m$ in this case. Both binarized 2D-Fourier transforms appear very similar in these figures where the model derived from Luneburg's kernel matches Fresnel's model. In both cases, these figures give the expected 2D-autocorrelation of the initial cross-like particle represented in figure 6.

Figure 12(a) shows the binarized 2D-Fourier transform of the decentred part of the interferometric pattern of figure 10(a) (selection of the pattern in the red rectangle), while 12(b) shows the binarized 2D-Fourier transform of the decentred part of the interferometric pattern of figure 10(b). Both binarized 2D-Fourier transforms appear very different in these figures where the model derived from Luneburg's kernel diverges from Fresnel's model. The shape's and size analysis can become erroneous using relation (1).

Finally, figure 13(a) shows the binarized 2D-Fourier transform of the whole interferometric pattern of figure 10(a), while 13(b) shows the binarized 2D-Fourier transform of the whole interferometric

pattern of figure 10(b). It appears that the non-respect of Fresnel conditions tends to shorten and sharpen the thin extremities of the 2D-Fourier transform of the pattern.

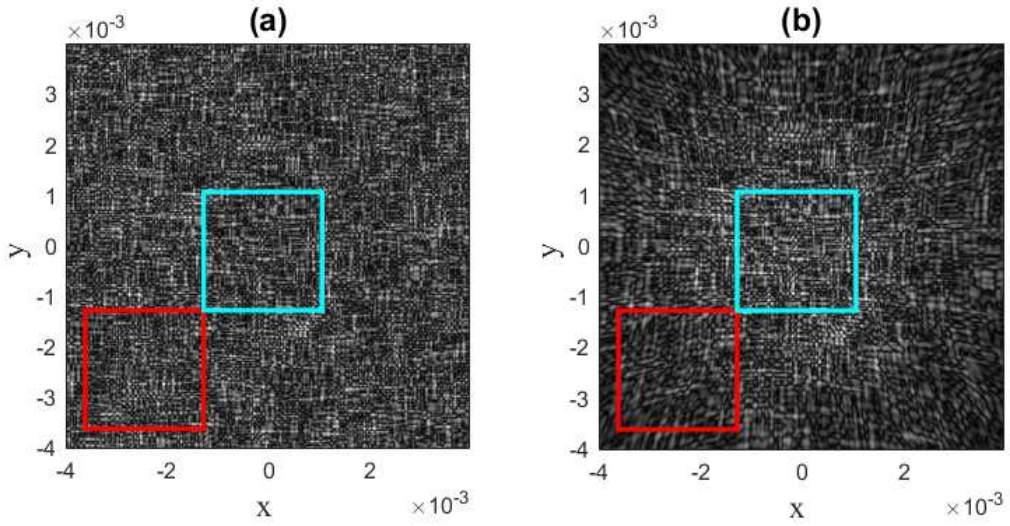

Figure 10: Interferometric images (actually the absolute value of the electric field for better contrast) of the cross-like particle of figure 6 using Fresnel's model (a) and Luneburg's model (b) at distance $z_p = 0.005m$.

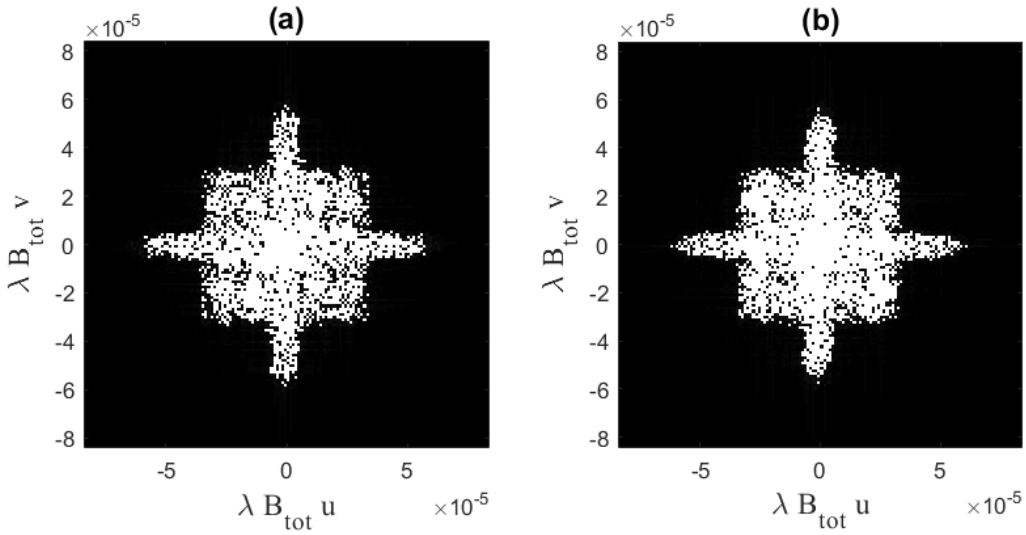

Figure 11: Binarized 2D-Fourier transform of the central part of the interferometric pattern of figure 10(a) (truncated pattern in the blue rectangle) (a), and of figure 10(b) (b).

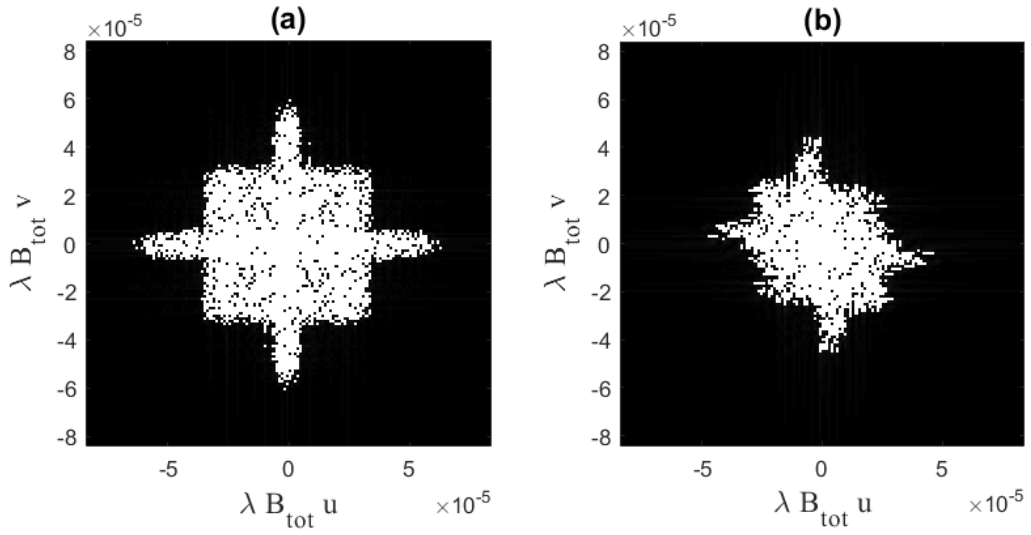

Figure 12: Binarized 2D-Fourier transform of the central part of the interferometric pattern of figure 10(a) (truncated pattern in the red rectangle) (a), and of figure 10(b) (b).

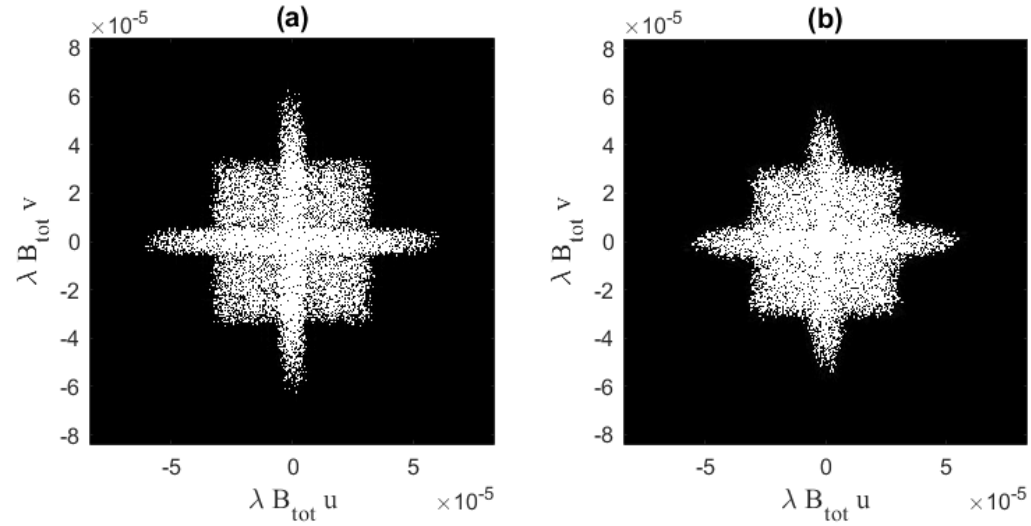

Figure 13: Binarized 2D-Fourier transform of the whole interferometric pattern of figure 10(a) (a), and of figure 10(b) (b).

IV – The potentiality of a vectorial model

The possibility to understand erroneous reconstructions is not the sole interest of this new model. As it is a vectorial model, it offers the possibility to describe the influence of light polarization on interferometric particle imaging experiments [34]. In figure 14, we plot the difference between the intensity pattern $I_{Fre}(x,y)$ obtained using the scalar equation (8) (Fresnel's model) and the intensity pattern $I_{Lu}(x,y)$ obtained using the vectorial model derived from Luneburg's kernel, based on relations (6) and (7). Figure 14 shows $|I_{Lu}(x,y) - I_{Fre}(x,y)|$ in four cases. In figure 14(a), the polarization of light scattered by the emitters is assumed to be linearly polarized along the bisector of axes x and y., i.e. $\boldsymbol{E_0} = \left(\frac{E_0}{\sqrt{2}}, \frac{E_0}{\sqrt{2}}, 0\right)$. In figure 14(b), the polarization is assumed to be linearly

polarized along the line of equation $y = -x/\sqrt{3}$, i.e. $\boldsymbol{E_0} = \left(\frac{\sqrt{3}\,E_0}{2}, -\frac{E_0}{2}, 0\right)$. In figure 14(c), it is assumed to be circularily polarized, i.e. $\boldsymbol{E_0} = \left(\frac{E_0}{\sqrt{2}}, \frac{i\,E_0}{\sqrt{2}}, 0\right)$. Finally, in figure 14(d), it is assumed to be elliptically polarized, i.e. $\boldsymbol{E_0} = \left(\frac{E_0}{\sqrt{2}}, -\frac{E_0}{\sqrt{2}}\,e^{i\,\pi/5}, 0\right)$ in this case. At distance $z_p = 0.005m$, $I_{Lu}(x, y, z_p)$ has been obtained from $I_{Lu}(x, y, z_p) \propto \left|E_{z_p}^x(x, y, z_p)\right|^2 + \left|E_{z_p}^y(x, y, z_p)\right|^2 + \left|E_{z_p}^z(x, y, z_p)\right|^2$ where the different components are given by relations (6) and (7). $I_{Fre}(x, y)$ has been obtained from relation (8). The plots of figure 14 do not show a significant role of the polarization. Luneburg and Fresnel models give similar results in the center of the patterns, while both models diverge when Fresnel conditions are no more respected. Nevertheless, the vectorial model enables to better understand the differences existing between the different cases. For example, figure 15 shows the z-component of the electric field $E_{z_p}^z(x, y, z_p)$ scattered in each of these four cases. Depending on the polarization of the light scattered, the domains of the speckle patterns where the longitudinal component of the electric field vanishes are different. In particular, for a linear polarization of the emitters, we can observe the linear domain of both speckle patterns where the longitudinal component of the scattered field vanishes.

These plots of figures 14 and 15 show simple examples of informations that can bring this vectorial model. We think that it can become a very powerful tool to describe interferometric particle imaging experiments where a pair of images are recorded for both transverse components x and y of polarization, and then analyzed separately for before comparison or combination of the results. With this formalism, it is possible to define emitters with different states of polarization, and thus to describe phenomenoms as Brewster incidence localized on specific points of the particle, depending on its shape, its local curvature and its roughness.

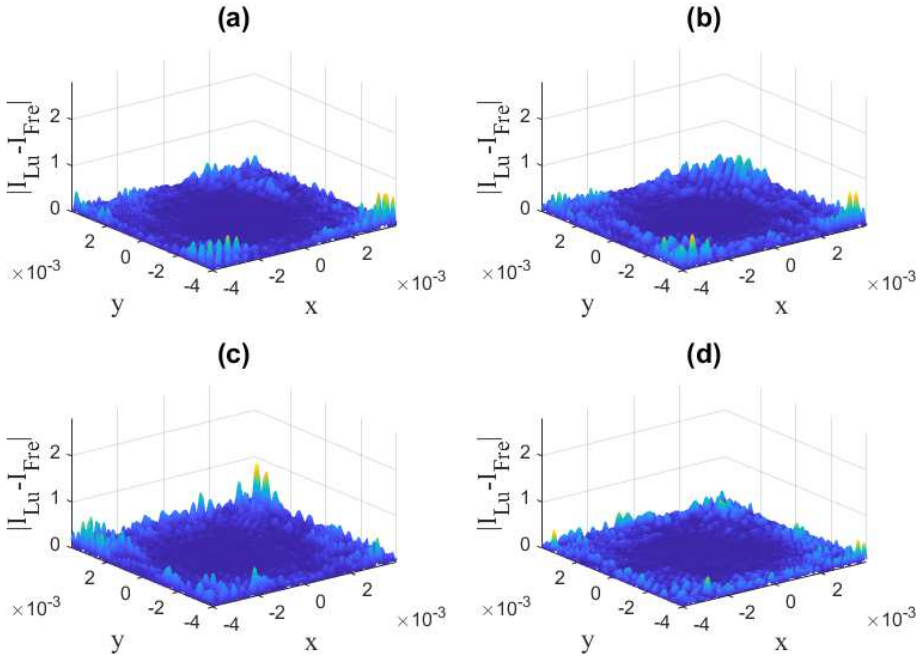

Figure 14: Normalized plots of the difference $|I_{Lu}(x, y) - I_{Fre}(x, y)|$ for different polarizations of the light scattered by the emitters: linear polarization along the bisector of axes x and y., i.e. $\boldsymbol{E_0} = \left(\frac{E_0}{\sqrt{2}}, \frac{E_0}{\sqrt{2}}, 0\right)$. (a), linear polarization along the line of equation $y = -x/\sqrt{3}$, i.e. $\boldsymbol{E_0} = \left(\frac{\sqrt{3}\,E_0}{2}, -\frac{E_0}{2}, 0\right)$

(b), circular polarization, i.e. $\boldsymbol{E_0} = \left(\frac{E_0}{\sqrt{2}}, \frac{i\,E_0}{\sqrt{2}}, 0\right)$ (c), elliptical polarization, i.e. $\boldsymbol{E_0} = \left(\frac{E_0}{\sqrt{2}}, -\frac{E_0}{\sqrt{2}}\, e^{i\,\pi/5}, 0\right)$ in this case (d)

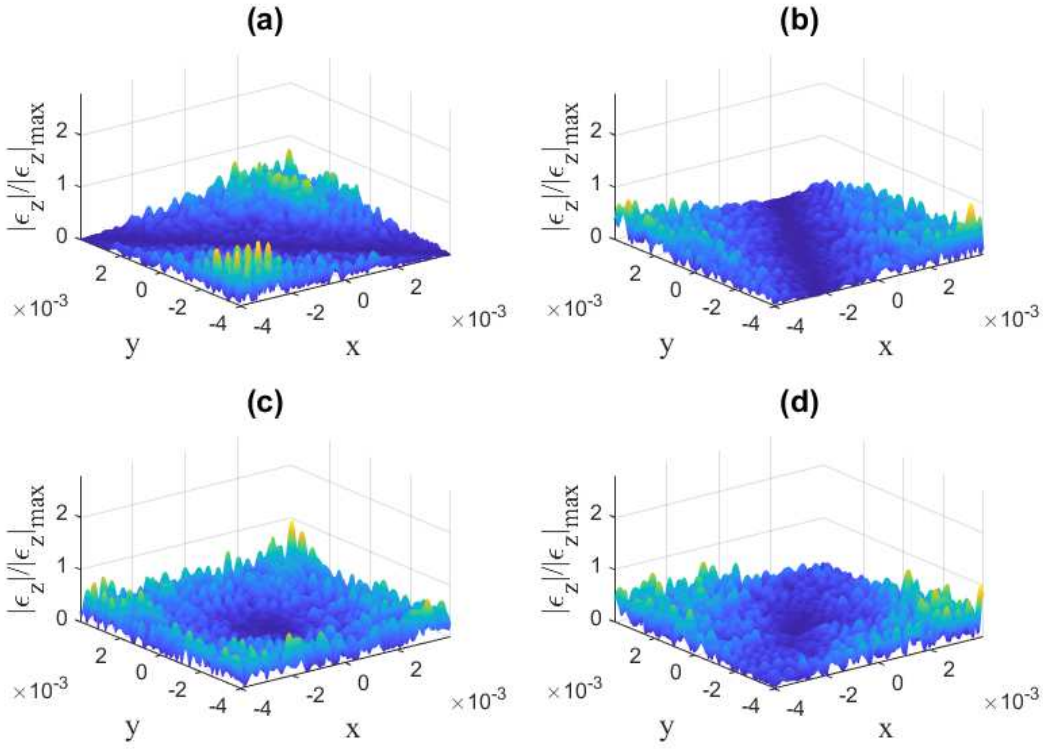

Figure 15: Longitudinal component of the electric field in the speckle patterns $E^z_{z_p}$, for different polarizations of the light scattered by the emitters : linear polarization along the bisector of axes x and y., i.e. $\boldsymbol{E_0} = \left(\frac{E_0}{\sqrt{2}}, \frac{E_0}{\sqrt{2}}, 0\right)$. (a), linear polarization along the line of equation $y = -x/\sqrt{3}$, i.e. $\boldsymbol{E_0} = \left(\frac{\sqrt{3}\,E_0}{2}, -\frac{E_0}{2}, 0\right)$ (b), circular polarization, i.e. $\boldsymbol{E_0} = \left(\frac{E_0}{\sqrt{2}}, \frac{i\,E_0}{\sqrt{2}}, 0\right)$ (c), elliptical polarization, i.e. $\boldsymbol{E_0} = \left(\frac{E_0}{\sqrt{2}}, -\frac{E_0}{\sqrt{2}}\, e^{i\,\pi/5}, 0\right)$ in this case (d)

Conclusion

The interferometric images of irregular rough particles are speckle patterns whose characteristics are directly correlated to the size and the morphology of the particle. An intense effort is done presently to proceed to efficient reconstructions of the particles from these speckle patterns. Reconstructions are based on direct methods as the hybrid input output or the error reduction algorithms, or on deep learning techniques [35-38]. In all cases, the description of the link between the particle's shape and its interferometric image is a key parameter for proper reconstruction. It is necessary to develop models as precise as possible that can describe the experimental conditions imposed by the imaging system. The vectorial model developed in this study, based on Luneburg's integral, should enable a very precise simulation of the patterns when experiments deliver results at the limit of validity of the Fresnel conditions. It offers further a vectorial description of the electric field scattered by the particles. It should be particularly useful for imaging experiments combining different states of

polarization. It will be further interesting in the future to study whether models based on an angular spectrum method can be convenient to describe IPI, for both droplets or bubbles and irregular rough particles.

References

[1] G. König, K. Anders, and A. Frohn, A new light-scattering technique to measure the diameter of periodically generated moving droplets, J. Aerosol Sci. 17 (1986) 157–167.
[2] R. Ragucci, A. Cavaliere, and P. Massoli, Drop sizing by laser light scattering exploiting intensity angular oscillation in the Mie regime, Part. Part. Syst. Charact. 7 (1990) 221–225.
[3] A. R. Glover, S. M. Skippon, and R. D. Boyle, Interferometric laser imaging for droplet sizing: a method for droplet-size measurement in sparse spray systems, Appl. Opt. 34 (1995) 8409–8421.
[4] T.Kawaguchi, Y. Akasaka, and M. Maeda, Size measurements of droplets and bubbles by advanced interferometric laser imaging technique, Meas. Sci. Technol. 13 (2002) 308–316.
[5] C. Mounaïm-Rousselle and O. Pajot, Droplet sizing by Mie scattering interferometry in a spark ignition engine, Part. Part. Syst. Charact. 16 (1999) 160–168.
[6] N. Damaschke, H. Nobach, and C. Tropea, Optical limits of particle concentration for multi-dimensional particle sizing techniques in fluid mechanics, Exp. Fluids 32 (2002) 143–152.
[7] S. Dehaeck and J. P. A. P. Van Beeck, Designing a maximum precision interferometric particle imaging set-up, Exp. Fluids 42 (2007) 767–781.
[8] Y. Hardalupas, S. Sahu, A. M. K. P. Taylor, and K. Zarogoulidis, Simultaneous planar measurement of droplet velocity and size with gas phase velocities in a spray by combined ILIDS and PIV techniques, Exp. Fluids 49 (2010) 417–434.
[9] H. Shen, S. Coëtmellec, G. Gréhan, M. Brunel, ILIDS revisited: elaboration of transfer matrix models for the description of complete systems, Appl. Opt. 51 (2012) 5357-5368.
[10] L. Qieni, H. Kan, G. Baozhen, and W. Xiang, High-accuracy simultaneous measurement of particle size and location using interferometric out-of-focus imaging, Opt. Express 24 (2016) 16530–16543.
[11] G. V. Kuznetsov, P. A. Strizhak, R. S. Volkov, and O. V. Vysokomornaya, Integral characteristics of water droplet evaporation in high-temperature combustion products of typical flammable liquids using SP and IPI methods, Int. J. Therm. Sci. 108 (2016) 218–234.
[12] S. V. Chvanov , and D. D. Andriyanov, Diagnostics of the Presence of Solid Particles in Aqueous Aerosol Droplets by Their Interference Pattern, Techn. Phys. Lett. 45 (2019) 605–608.
[13] Y. Wu, H. Li, M. Brunel, J. Chen, G. Gréhan, and L. Madler, Phase interferometric particle imaging (PHIPI) for simultaneous measurements of micron-sized droplet and nanoscale size changes, Appl. Phys. Lett. 111 (2017) 041905.
[14] A.García-Magariño, S.Sor, R.Bardera, J.Muñoz-Campillejo, Interferometric laser imaging for droplet sizing method for long range measurements, Measurement (2021) 108418.
[15] M. Brunel, H. Shen, S. Coëtmellec, G. Gréhan, T. Delobel , Determination of the size of irregular particles using interferometric out-of-focus imaging, International Journal of Optics, (2014) 143904.

[16] M. Brunel, S. Gonzalez Ruiz, J. Jacquot, J. van Beeck, On the morphology of irregular rough particles from the analysis of speckle-like interferometric out-of-focus images. Opt. Commun. 338 (2015) 193-198.
[17] González Ruiz S., van Beeck J., Sizing of sand and ash particles using their speckle pattern: influence of particle opacity, Exp. Fluids 58 (2017) 100.
[18] H. Zhang, Z. Li, J. Li, X. Wang, D. Jia, and T. Liu, Simultaneous shape and size measurements of irregular rough particles by an IPI system with double receivers, J. Mod. Opt. 66 (2019) 1226–1234.
[19] X. Wu, L. Shi, Z. Lin, Y. Wu, M. Brunel, J. Jacquot, G. Gréhan, Dual-beam interferometric particle imaging for size and shape characterization of irregular coal micro-particle: validation with digital inline holography, J. Quant. Spectrosc. Radiat. Transf. 241 (2020) 106728.
[20] Y. Wu, Y. Gong, L. Shi, Z. Lin, X. Wu, C. Gong, Z. Zhou, Y. Zhang, Backward interferometric speckle imaging for evaluating size and morphology of irregular coal particles, Opt. Commun. 491 (2021) 126957.
[21] M. Brunel, M. Talbi, S. Coetmellec, G. Gréhan, Y. Wu, J. Jacquot, Interferometric out-of-focus imaging of freezing droplets, Opt. Commun. 433 (2019) 173-182.
[22] M. Talbi, R. Duperrier, B. Delestre, G. Godard, M. Brunel, Interferometric ice particle imaging in a wind tunnel, Optics 2 (2021) 216–227.
[23] K.G. Libbrecht, The physics of snow crystals. Rep. Prog. Phys. 68 (2005) 855.
[24] R. K. Luneburg. Mathematical theory of optics. University of California Press, 1964.
[25] L. Carretero, P. Acebal, and S. Blaya. Diffraction of convergent spherical waves with all possible polarization states usingthe luneburg integral method. J. Opt. Soc. Am. A 30 (2013) 733–740.
[26] S. Coëtmellec, D. Lebrun, M. Brunel and A. J. E. M. Janssen, Assessment about Luneburg integrals and application to digital in-line holography, J. Europ. Opt. Soc.: Rap. Public 17 (2021) 12.
[27] H. Shen, S. Coëtmellec, M. Brunel, Simultaneous 3D location and size measurement of spherical bubbles using cylindrical interferometric out-of-focus imaging, J. Quantum Spectrosc. Radiat. Transfer 131 (2013) 153-159.
[28] J. Jacquot, M. Talbi, M. Brunel, Third glare point effect in 90° Interferometric Laser Imaging for Droplet Sizing, Opt. Commun. 462 (2020) 125349.
[29] Brunel M., Shen H., Design of ILIDS configurations for droplet characterization, Particuology, 11 (2013) 148-157.
[30] M. Brunel, S. Coetmellec, G. Gréhan, H. Shen, Interferometric out-of-focus imaging simulator for irregular rough particles, J. Europ. Opt. Soc.: Rap. Public. 9 (2014) 14008.
[31] E. Porcheron, P. Lemaitre, J. van Beeck, R. Vetrano, M. Brunel, G. Gréhan, L. Guiraud, Development of a spectrometer for the airborne measurement of droplet sizes in clouds, J. Europ. Opt. Soc.: Rap. Public 10 (2015) 15030.
[32] C. Palma and V. Bagini, Extension of the Fresnel transform to ABCD systems, J. Opt. Soc. Am. A 14 (1997) 1774–1779.
[33] J. J. Wen and M. Breazeale, A diffraction beam expressed as the superposition of Gaussian beams, J. Acoust. Soc. Am. 83 (1988) 1752–1756.
[34] H. Zhang, M. Zhai, J. Sun, D. Jia, T. Liu, Y. Zhang, Discrimination between spheres and spheroids in a detection system for single particles based on polarization characteristics, J. Quantum Spectrosc. Radiat. Transfer 187 (2017) 62-75.

[35] R. Fienup, T.R. Crimmins, W. Holsztynski, Reconstruction of the support of an object fro the support of its autocorrelation, J. Opt. Soc. Am. 7 (1982) 3-13.
[36] H. Shen, L. Wu, Y. Li, W. Wang, Two-dimensional shape retrieval from the interferometric out-of-focus image of a nonspherical particle – Part I:theory, Appl. Opt. 57 (2018) 4968-4976.
[37] B. Delestre, A. Abad, M. Talbi, M. Fromager, M. Brunel, Experimental particle's shapes reconstructions from their interferometric images using the Error-Reduction algorithm, Opt. Commun. 498 (2021) 127229.
[38] H. Zhang, Z. Li, J. Sun, Y. Fu, D. Jia, T. Liu, Characterization of particle size and shape by an IPI system through deep learning, J. Quantum Spectrosc. Radiat. Transfer 268 (2021) 107642.